(Received 14 May 2024, Accepted 8 July 2024, Scheduled 15 July 2024)

# Flexible Discretization of Singular Green Functions Using a Composite Spectral Integration Path

Daan van den Hof*, Martijn C. van Beurden, and Roeland J. Dilz

*Department of Electrical Engineering, Eindhoven University of Technology, The Netherlands*

**ABSTRACT:** Scattering of electromagnetic waves by a dielectric object can be described as an integral equation involving a Green function. These types of problems can be solved using a spatial spectral formulation, which requires sampling of the spectral Green function. To avoid sampling around the singularities on or near the real axis, the spectral Green function is represented on three separate complex paths. Using appropriate selection functions, these paths are recombined such that the original Fourier integrals are retrieved. This composite path method provides a general way to solve domain integral equations involving Green functions with simple singularities with minimal computational overhead.

## 1. INTRODUCTION

The field of computational electromagnetics (EM) is concerned with methods to approximate numerical solutions to Maxwell's equations in different settings. A subclass of EM problems is finding the scattered field given an incident wave and the description of a scatterer. To this end, a broad class of methods have been developed, each of which makes different choices in the formulation of the problem. One such choice is between a time-domain (for example FDTD [1], FETD [2]) or a frequency-domain approach. In this work we are interested in the latter. Another choice to make is between a local and a global approach. Direct discretization of the differential form of Maxwell's equations leads to local methods like the finite element methods (FEM), see, e.g., [3]. Generally, these methods work by setting up a system of equations comprising the interactions between neighbouring domains and then solving the system. In contrast, global methods seek to solve the EM fields at an arbitrary point in some potentially unbounded domain. In particular, Green-function-based methods for a homogeneous background medium allow the EM fields to be calculated at any point using a convolution integral. Instead of computing this integral directly, we can perform a multiplication in the spectral domain between the Green function and a contrast current density [4–6]. In [7, 8], a "spatial spectral" method was proposed to solve scattering problems in layered media. In that work, Gabor frames were used since they provide simple (inverse) Fourier transformations.

In [9], a Hermite interpolation was used to replace the Gabor frame. The interpolation method defined a set of basis functions as well as the operations concerning addition, multiplication, and Fourier transformation. The Hermite interpolation was chosen over the Gabor frames owing to their simpler multiplications at the cost of somewhat more complex and less-accurate Fourier transforms.

Especially for layered media, representing the Green function in terms of smooth functions, like a Gabor frame, is challenging, because in the spectral domain, the Green function contains poles and branch cuts [10]. A transformation to the spatial domain is not straightforward, since it requires the computation of time-consuming Sommerfeld-integrals [10–12].

Therefore, in [8] a path-deformation of the spectral domain into the complex plane was used, which circumvents the poles and branch cuts in the Green function. However, the downside of this method in the spatial spectral solver is that in two dimensions, four copies of the spectral domain were required, and to correctly capture the long-distance behavior of the Green function, these four copies required double the spatial extent of the original scattering problem in both directions. This leads to more than a 16-fold increase in memory usage and computation time as compared to operations on the real-axis spectral domain. Additionally, the implementation of this complex integration path requires an intricate and somewhat fragile procedure to piece together different parts of the path, which requires many simulation parameters to be optimized. In [9], a more robust path-deformation was implemented for the spectral coordinate. By approximating the resulting extra exponential term under the Fourier integrals by an order $N$ Taylor expansion, the Fourier and inverse Fourier transformations corresponding to this path are approximated by a sum of $N$ regular Fourier integrals. This method leads to a very simple Green function representation that does not require sampling around the poles and branch-cuts, resulting in a clean formulation at the cost of additional computational costs since in practice $N$ can be quite large (e.g., 8 or more).

An earlier approach that utilized a spatial spectral approach is Ewald summation [13, 14], and in that method the near- and far-field interactions of the Green functions are separated in rapidly converging representations in the spatial and spectral domains. However, this approach is only valid for periodic problems. To

* Corresponding author: Daan van den Hof (d.van.den.hof@tue.nl).

us, it is interesting that such a separation allows to efficiently represent long-distance interactions by only considering the behavior of the Green function around its poles and branch cuts.

We propose a method for solving a-periodic scattering problems where only the long-distance behavior of the Green function is sampled on the spectral-domain path, leading to the same clean formulation but with computation times and memory costs closer to those of a non-deformed path. We demonstrate this principle on a 2D $E$-polarized setup with simple homogeneous dielectric cylindrical scatterers. However, the underlying principles are extendable to Green functions with comparably simple singularities, similar to the extension from the case of 2D $E$-polarization in [8] to the full 3D case in [15]. To achieve this, we represent the spectral-domain Green function on three separate complex paths, two of which have an imaginary offset. In this way, the singularities on or close to the real axis can be avoided, and we can represent the full Green function by combining different sections of the paths. This approach separates the long- and short-range interactions, since the spectral singularities are treated separately in the paths with imaginary offset. This separation allows for optimization, since we can choose different discretization parameters for different parts of the paths, and a rather coarse sampling suffices for the long-range interaction.

In Section 2, we briefly introduce the $E$-polarized two-dimensional (scalar) scattering problem statement and the high-level approach towards solving it. We set up a general discretization framework in Section 3 that we use as a basis to formulate this problem in. We go over the details of the implementation of this framework and the choice of simulation parameters in Section 4. In Section 5, we demonstrate the spectral deformation method for several setups. We quantify the accuracy of our method using simple dielectric cylinders and show that the method generalizes to more complicated setups by computing the fields scattered by a dielectric lens. Finally, we draw conclusions in Section 6.

## 2. PROBLEM STATEMENT AND ANALYSIS

We consider a time-harmonic EM scattering problem in a 2D $E$-polarized configuration with a compactly supported dielectric scatterer placed in an isotropic homogeneous background with permittivity $\epsilon_0$ and permeability $\mu_0$, Fig. 1. The scatterer is described by the contrast function

$$\Pi(\vec{x}) = \epsilon_r(\vec{x}) - 1, \tag{1}$$

where $\epsilon_r(\vec{x})$ is the relative permittivity with respect to the background medium. The scatterers in this work are homogeneous cylinders. For this class of problems there are existing methods that lead to fast and accurate solutions, e.g., the T matrix [16]. However, our analysis is not limited to such cases. In principle the scatterer can have any arbitrary shape, can consist of multiple smaller scatters and can have any $\epsilon_r$ profile. Our approach will make frequent use of both spatial and spectral versions of functions, where one is given by the 2D (inverse) Fourier transformation of the other. For the forward and inverse transformations, we use the operators $\mathcal{F}$ and $\mathcal{F}^{-1}$, respectively,

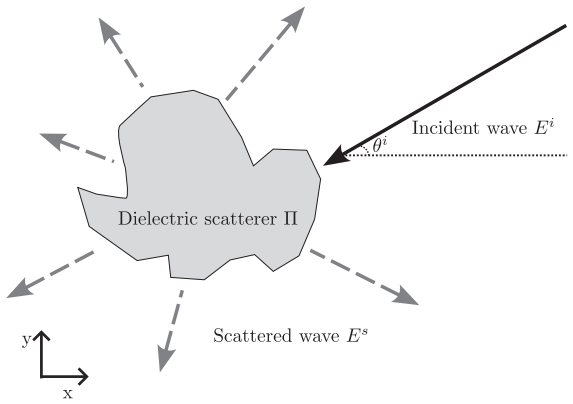


**FIGURE 1**. Schematic setup of the 2D $E$-polarized scattering problem.

and we use the following convention:

$$\begin{aligned}\mathcal{F}\Big\{f(\vec{x})\Big\}(\vec{k}) &= \frac{1}{2\pi}\int_{-\infty}^{\infty}\int_{-\infty}^{\infty} f(\vec{x})e^{-j\vec{k}\cdot\vec{x}}dxdy,\\ \mathcal{F}^{-1}\Big\{\hat{f}(\vec{k})\Big\}(\vec{x}) &= \frac{1}{2\pi}\int_{-\infty}^{\infty}\int_{-\infty}^{\infty} \hat{f}(\vec{k})e^{j\vec{k}\cdot\vec{x}}dk_xdk_y,\end{aligned} \tag{2}$$

where we have introduced spatial and spectral coordinate vectors:

$$\begin{aligned}\vec{x} &= [x, y]^T \text{ (spatial)},\\ \vec{k} &= [k_x, k_y]^T \text{ (spectral)}.\end{aligned} \tag{3}$$

Furthermore, we indicate the spectral counterpart to a spatial function $f(\vec{x})$ as $\hat{f}(\vec{k})$.

Following [17] and using $e^{j\omega t}$ for the time convention, the scattering problem can be described by the integral equation

$$E^i(\vec{x}) = E(\vec{x}) - \frac{k_0^2}{j\omega\epsilon_0}\int_D G(\vec{x}-\vec{x}')J(\vec{x}')d\vec{x}'. \tag{4}$$

Here, $k_0 = \omega\sqrt{\epsilon_0\mu_0}$ is the wavenumber, and $G$ is the spatial-domain Green function given by

$$G(\vec{x}) = -\frac{j}{4}H_0^{(2)}\left(k_0\sqrt{x^2+y^2}\right). \tag{5}$$

The contrast current density $J(\vec{x})$ is given by

$$J(\vec{x}) = j\omega\epsilon_0\Pi(\vec{x})E(\vec{x}), \tag{6}$$

with $E(\vec{x})$ the total electric field that can be decomposed into the incident ($E^i(\vec{x})$) and scattered ($E^s(\vec{x})$) electric fields as

$$E(\vec{x}) = E^i(\vec{x}) + E^s(\vec{x}). \tag{7}$$

By employing a Fourier transformation, the spatial convolution in Eq. (4) can be performed in the spectral domain via straightforward multiplication. Hence, we can restate the scattering problem as

$$E^i(\vec{x}) = E(\vec{x}) - 2\pi k_0^2\mathcal{F}^{-1}\Big\{\hat{G}(\vec{k})\mathcal{F}\Big\{\Pi(\vec{x})E(\vec{x})\Big\}\Big\}, \tag{8}$$

which is the spatial spectral form that we will be using to solve the problem. The 2D $E$-polarized spectral-domain Green function corresponding to Eq. (5) is given by [17]

$$\hat{G}(\vec{k}) = \frac{1}{2\pi\left(k_x^2 + k_y^2 - k_0^2\right)}. \tag{9}$$

### 2.1. General Solution Strategy

The formulation in Eq. (8) is used to numerically solve the scattering problem. First, numerical representations for $\hat{G}(\vec{k})$, $E^i(\vec{x})$, and $\Pi(\vec{x})$ are constructed. Then, an iterative solver is employed to solve the pertaining linear system to obtain an approximation for the total electric field. However, setting up these numerical representations is not a trivial process, especially for the spectral Green function, Eq. (9), in view of its singularity on the circle with radius $k_0$ centered at the origin in the $k_x$-$k_y$ plane.

### 2.2. A Three-path Representation of the Spectral Green Function

Previously, in [8, 9], the spectral Green function was formulated in the spectral domain using a deformed integration path that avoided the singularities. Using such a formulation the Green function can be directly represented by a Hermite-interpolation-based discretization. These methods had the downside of requiring the discretization range to be twice the largest dimension of the scatterer. Both methods also required additional computational overhead, the first needing extra copies of the spectral domains and the second requiring an order $N$ Taylor approximation meaning that each overall Fourier transformation required $N$ total sub-transformations. Here, we introduce a composite path which allows for the same flexibility in representation while also providing the possibility to a separate discretization for the regions around the singularities from the rest of the spectral Green function. This is more efficient since it does not require the same level of redundancy required by either previous method. We will go over this formulation here and discuss the discretization process itself in Section 3.

For the analysis, we will restrict ourselves to the case where $k_y = 0$. Since the discretization dimensions are independent, this can be generalized to the full 2D case without changing much about the analysis, and the extra considerations for the 2D case are discussed in 4.6. For this case, we have the following spectral Green function

$$\begin{aligned}\hat{G}(k_x) &= \frac{1}{2\pi\left(k_x^2 - k_0^2\right)} \\ &= \frac{1}{4\pi k_0}\left(\frac{1}{k_x - k_0} - \frac{1}{k_x + k_0}\right).\end{aligned} \tag{10}$$

This function contains simple poles at $k_x = \pm k_0$. To avoid sampling this function near these poles, we construct a composite path representation. Supposing that we have an analytic function $f(k)$, we can rewrite this as

$$\begin{aligned}\hat{f}(k) &= \left(\hat{s}_m(k) + \hat{s}_l(k) + \hat{s}_r(k)\right)\hat{f}(k) \\ &= \hat{f}_m(k) + \hat{f}_l(k) + \hat{f}_r(k)\end{aligned} \tag{11}$$

where the selection functions $\hat{s}_m(k_x)$, $\hat{s}_l(k_x)$, and $\hat{s}_r(k_x)$ constitute a partition of unity. The subscripts are short for "main", "left", and "right". The selection functions are chosen such that $\hat{f}_m(k_x) \approx \hat{f}(k_x)$ for all $k_x$ except in a small region around $k_x = \pm k_0$. The side functions $\hat{s}_l(k_x)$ and $\hat{s}_r(k_x)$ are (close to) 0 everywhere, except for a small region around the corresponding singularity of the spectral Green function. We choose these side functions to be symmetric so $\hat{s}_l(k_x) = \hat{s}_r(-k_x)$. An example of one of these functions is shown in Fig. 2.

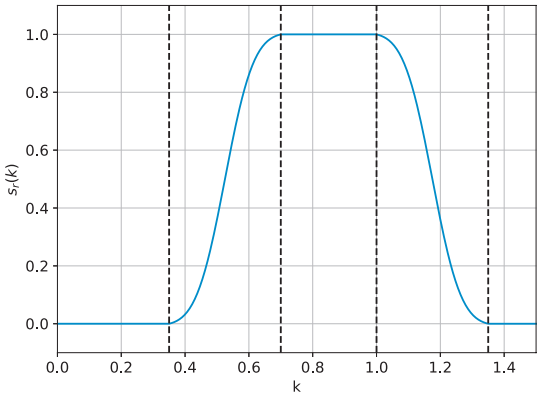


**FIGURE 2**. An example of a graph for $s_r(k)$. Ideally the function is zero everywhere except for a finite region around $k_0$.

For the analysis we assume that the selection functions are also analytic, to allow for contour deformations of the integration path. For analytic selection functions, we can use the property

$$\hat{f}(k_x + jA) = \mathcal{F}\Big\{\exp(Ax)f(x)\Big\}, \tag{12}$$

to add an offset $jA$, with $A \in \mathbb{R}$, to the path on which $\hat{f}_l(k)$ and $\hat{f}_r(k)$ are represented. If this is done for the Green function, the poles will be avoided when sampling. Most functions we want to represent are bounded and vanish as $k \to \infty$. For these functions we can obtain the complete composite path representation in the spatial domain as

$$\begin{aligned}f(x) &= \mathcal{F}^{-1}\Big\{\hat{f}_m(k)\Big\} + e^{Ax}\mathcal{F}^{-1}\Big\{\hat{f}_l(k - jA)\Big\} \\ &\quad + e^{-Ax}\mathcal{F}^{-1}\Big\{\hat{f}_r(k + jA)\Big\}.\end{aligned} \tag{13}$$

For an unbounded spectral-domain function, like the Green function, this property is not guaranteed to hold. In view of the chosen time-convention, the integration path used in $\mathcal{F}^{-1}\Big\{\hat{G}(k)\Big\}$ needs to evade the poles and pass underneath the pole at $k = -k_0$ and over the pole at $k = k_0$, for the resulting Green function to correspond to the outgoing-wave solution and satisfy the radiation condition [12]. The functions we are dealing with are assumed to be analytic, except for simple poles at known locations. Therefore, the Fourier integral will yield the same result regardless of the integration path, as long as the endpoints remain the same, and the singularities are evaded on the appropriate side. This principle is shown in Fig. 3. From

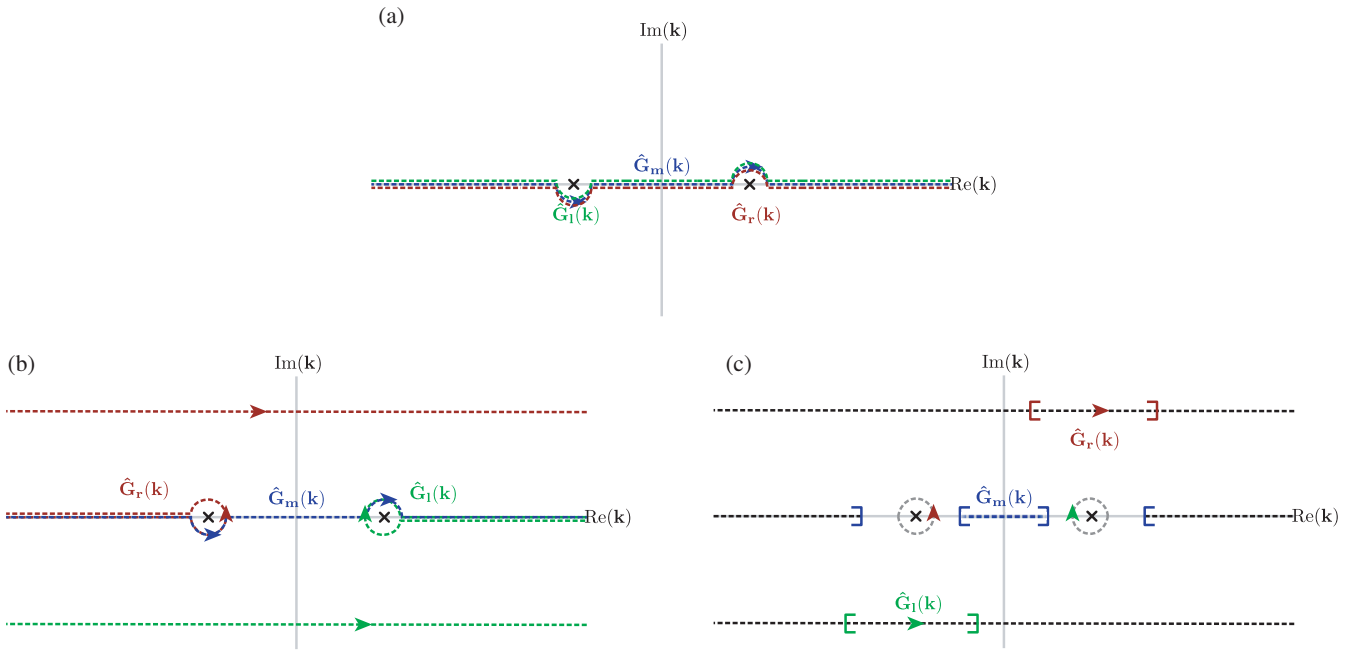


**FIGURE 3**. (a) The integration path for the inverse Fourier transformation corresponding to the outgoing-wave solutions to the wave equation for $m$, $l$, and $r$ of the representation in Eq. (11). (b) Since the function is analytic everywhere except at the two poles, the value of the integral does not change, as long as we evade the poles on the correct sides. We choose different paths for the integrals on the $l$ and $r$ parts. (c) The Green function can be represented by adding the contributions of the three parts where their respective selection functions are non-negligible.

this we conclude that (13) also holds for $\hat{G}(k)$. By choosing $\hat{G}_l(k)$, $\hat{G}_r(k)$, and $\hat{G}_m(k)$ to be represented each on a different path, such that the poles are not contained in the support of their respective selection functions, we obtain a well behaved three-path representation for the Green function.

## 3. DISCRETIZATION

The analysis so far concerned a continuous context. However, in practice the problem is to be solved numerically. To do this, we construct discrete analogs to the required functions, e.g., $\hat{G}(k)$, as well as the operators acting on them. We developed software, written in C++ and compiled as a Python library, to implement this discretization process. The goal in developing this software is to have it be both flexible and efficient. To do this we set up a strict paradigm to which we adhere in the implementation.

We define two types of structures, a *data object* and a *discretization object*. A data object is generic: it only contains data representing a function and a reference to an associated discretization object. A data object representing a function $f$, using a discretization object $d$, is denoted as $\mathbb{f}_d$ for the spatial domain or $\hat{\mathbb{f}}_d$ for the spectral domain. A discretization object contains the actual logic used to create and manipulate data objects. This hierarchy is depicted in Fig. 4.

By making this conceptual split, we can use the data objects as a front-end and have them call their discretization objects when needed. This means adaptations to discretization objects, for example adding new types, can be performed completely independently from the data objects, which provides flexibility in implementation while keeping the front-end intact.

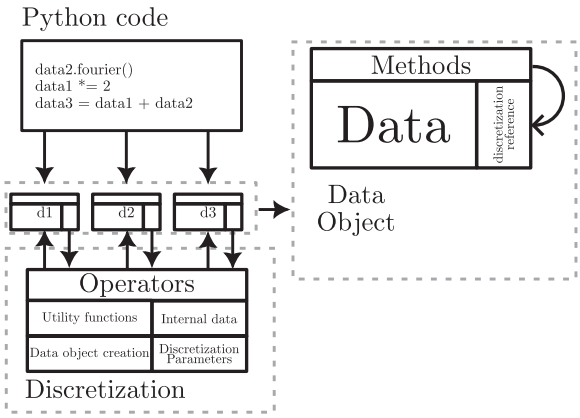


**FIGURE 4**. The data objects act as a generic front-end interface to the code. The actual logic to make use of these objects is implemented by their associated discretization objects.

Every discretization object is specified by a set of parameters, e.g., sample distance, that are given at initialization. In the software we always require a separate discretization object for both the spatial and spectral domains since this is required for the spatial spectral solver. In practice, the spatial domain parameters are provided by the user while the corresponding spectral domain parameters are derived from them. We only discuss the 1D case in detail. Higher dimensional problems can be solved by "stacking" 1D discretization objects: e.g., a 2D problem would have one discretization object for the $x$ and one for the $y$ direction.

**TABLE 1.** Parameters for the Hermite discretization.

| Hermite discretization $h$ | Spatial | Spectral |
|---|---|---|
| Sample distance | $\Delta_x$ | $\Delta_k$ |
| Sampling range | $r_x$ | $r_k$ |
| Interpolation order | d | d |

### 3.1. The Hermite Discretization Object

In [9], the spatial spectral method was implemented using Hermite interpolation at the core of the discretization object. We build on this work to construct a composite discretization object (CDO) that can be used to implement Eq. (13). The behavior of the Hermite discretization object is determined by the parameters shown in Table 1. The spatial and spectral parameters are related through

$$\begin{aligned} \Delta_k &\approx \frac{\pi}{r_x}, \\ r_k &\approx \frac{\pi}{\Delta_x}. \end{aligned} \tag{14}$$

The data objects for this discretization method contain values that represent a function and derivatives up to order $d-1$ of that function, sampled on a symmetric grid at $2N+1$ points:

$$\begin{aligned} \mathbb{f}_d &\equiv \left\{ f^{(m)}(n\Delta_x) \middle| \begin{matrix} n \in \{-N, \ldots, N\} \\ m \in \{0, \ldots, d-1\} \end{matrix} \right\}, \\ \hat{\mathbb{f}}_d &\equiv \left\{ \hat{f}^{(m)}(n\Delta_k) \middle| \begin{matrix} n \in \{-N, \ldots, N\} \\ m \in \{0, \ldots, d-1\} \end{matrix} \right\}. \end{aligned} \tag{15}$$

When referring to a specific entry of the data object, we use the following notation: $\mathbb{f}_d[n, m]$, where $n$ is the location index, and $m$ is the derivative index. If we want to get an approximate value for the function in between the samples, we use the Hermite interpolation:

$$f(x) \approx \sum_{n=-N}^{N} \sum_{m=0}^{d-1} b_{nm}(x) \mathbb{f}_d[n, m]. \tag{16}$$

The form of the piecewise polynomial basis functions $b_{nm}(x)$ can be found in [9]. To actually use the data objects, a set of operators needs to be implemented. Addition of data objects is performed by element-wise addition of the individual objects, i.e., $\mathbb{f}_d = \mathbb{g}_d + \mathbb{h}_d$:

$$\left\{ \mathbb{f}_d[n, m] = \mathbb{g}_d[n, m] + \mathbb{h}_d[n, m] \right\}. \tag{17}$$

To multiply two data objects, i.e., $\mathbb{f}_d = \mathbb{g}_d \cdot \mathbb{h}_d$, we use the general Leibniz rule, i.e.,

$$\left\{ \mathbb{f}_d[n, m] = \sum_{l=0}^{m} \binom{m}{l} \mathbb{g}_d[n, m] \mathbb{h}_d[n, m-l] \right\}. \tag{18}$$

This ignores the terms of derivative orders higher than $m$, which is necessary to keep the interpolation degree the same. Another required operation is the inner product, and for the Hermite discretization this is obtained by

$$\langle \mathbb{f}_d, \mathbb{g}_d \rangle = \sum_{n=-N}^{N-1} \sum_{i=0}^{d-1} \sum_{j=0}^{d-1} \sum_{k=-1}^{1} c_{ijnk} \mathbb{f}_d[n, i] \overline{\mathbb{g}_d}[n+k, j], \tag{19}$$

where $\overline{\mathbb{g}_d}$ denotes the complex conjugation. The coefficients $c_{ijnk}$ are determined by

$$c_{ijnk} = \int_{-\infty}^{\infty} b_{ni}(x) b_{(n+k)j}(x) dx. \tag{20}$$

See Table 2 for a summary of all the operators for the Hermite discretization.

**TABLE 2.** The operators implemented by the Hermite discretization objects.

| Operator name | Notation | Description |
|---|---|---|
| Sampling | $\mathcal{S}_d(f(x)) = \mathbb{f}_d$, $\mathcal{S}_{\hat{d}}(f(k)) = \hat{\mathbb{f}}_d$ | Sample a function and its first $d-1$ derivatives and store the values in a data object (Eq. (15)). |
| Addition | $\mathbb{a}_d = \mathbb{b}_d + \mathbb{c}_d$ | Add two data objects together into a third one (Eq. (17)). |
| Multiplication | $\mathbb{a}_d = \mathbb{b}_d \cdot \mathbb{c}_d$ | Multiply two data objects together into a third one (Eq. (18)). |
| Scalar multiplication | $\mathbb{a}_d = b\mathbb{c}_d$ | Multiply a data object by a scalar. |
| Fourier transformation | $\mathcal{F}_d\left\{\mathbb{f}_d\right\} = \hat{\mathbb{f}}_{\hat{d}}$, $\mathcal{F}^{-1}_{\hat{d}}\left\{\hat{\mathbb{f}}_{\hat{d}}\right\} = \mathbb{f}_d$ | Perform an (inverse) Fourier transformation ([9], Eq. (12)]. |
| Interpolation | $\mathcal{E}_d(\mathbb{f}_d, x)$ | Use the Hermite interpolation Eq. (16) to get the approximate value of $f$ by using the Hermite basis expansion. |
| Re-sampling | $\mathcal{R}_{d2}(\mathbb{f}_d, a) = \mathcal{S}_{d2}\left(\mathcal{E}_d(\mathbb{f}_d, x+a)\right)$ | Interpolate a data object and use the values to create a data object with a different discretization object. The parameter $a$ refers to an optional shift in the representation. |
| Inner product | $\langle \mathbb{f}_c \mathbb{g}_d \rangle$ | Take the inner product of two data objects Eq. (19). |

### 3.2. The Composite Discretization Object

In Section 2.2, we constructed a representation for the Green function that does not require direct sampling around the singularities. To implement this representation into our solver, we

introduce a new type of composite discretization object (CDO) that consists of three separate Hermite discretization objects: main ($m$), left ($l$), and right ($r$). When the latter two are talked about together, we refer to both of them as "side" ($s$) discretization objects. We indicate the discretization associated with an operator or data object using subscripts. For example, sampling into a CDO $\hat{d}$ is written as

$$\hat{\mathbb{f}}_{\hat{d}} = \mathcal{S}_{\hat{d}}(\hat{f}) \tag{21}$$

whereas for the individual (Hermite) component objects we write

$$\begin{aligned}\hat{\mathbb{f}}_{\hat{d}l} &= \mathcal{S}_{\hat{d}l}(\hat{f}),\\ \hat{\mathbb{f}}_{\hat{d}r} &= \mathcal{S}_{\hat{d}r}(\hat{f}),\\ \hat{\mathbb{f}}_{\hat{d}m} &= \mathcal{S}_{\hat{d}m}(\hat{f}).\end{aligned} \tag{22}$$

The left and right discretization objects are used to represent data around the singularities in the spectral domain, whereas the main discretization object is used for all other data. This means that all three discretization objects are needed in the spectral domain, while in the spatial domain only $\mathbb{f}_{dm}$ is required, with the exception of the Fourier transformations.

To implement the composite path representation within a discretization object we, require a method to meaningfully combine the component discretization objects without redundant information. To this end we use sampled versions of Eq. (11):

$$\begin{aligned}\hat{\mathbb{s}}_{\hat{d}m} &= \mathcal{S}_{\hat{d}m}(s_{\hat{d}m}(k)),\\ \hat{\mathbb{s}}_{\hat{d}l} &= \mathcal{F}_{dl}\Big\{\mathbb{e}^{(1)}_{dl}\cdot\mathcal{F}^{-1}_{\hat{d}l}\Big\{\mathcal{S}_{\hat{d}l}(s_{\hat{d}l}(k-z))\Big\}\Big\},\\ \hat{\mathbb{s}}_{\hat{d}r} &= \mathcal{F}_{dr}\Big\{\mathbb{e}^{(2)}_{dr}\cdot\mathcal{F}^{-1}_{\hat{d}r}\Big\{\mathcal{S}_{\hat{d}r}(s_{\hat{d}r}(k+z))\Big\}\Big\},\end{aligned} \tag{23}$$

where we introduced a shift $z\in\mathbb{R}^+$, in the side discretization objects. This shift is added to improve computational efficiency by reducing the Nyquist sample rate and is discussed in more detail in Section 4.5. The exponential function data objects are given by:

$$\mathbb{e}^{(1)}_{dl} = \mathcal{S}_{\hat{d}l}(\exp(-Ax)), \tag{24}$$

and

$$\mathbb{e}^{(2)}_{dr} = \mathcal{S}_{\hat{d}r}(\exp(Ax)). \tag{25}$$

These functions implement the complex shift corresponding to Eq. (12).

### 3.3. CDO Operators

We decided that the data objects should be generic and should be usable in the same manner, regardless of the underlying discretization objects. For this reason the operators for the CDO should have the same structure and syntax as the Hermite discretization object.

Of these operators, addition, multiplication, and scalar multiplication are trivially extended, and they can be executed component wise. For example, for addition we have

$$\mathbb{f}_d + \mathbb{g}_d \to \big\{(\mathbb{f}_{dl}+\mathbb{g}_{dl}),(\mathbb{f}_{dr}+\mathbb{g}_{dr}),(\mathbb{f}_{dm}+\mathbb{g}_{dm})\big\}. \tag{26}$$

In the spatial domain, sampling, interpolation, re-sampling, and taking the inner product are also trivial since they involve the main part of the discretization only and are thus inherited from the underlying Hermite discretization object. In the spectral domain, sampling only requires shifting the argument of the function in question:

$$\begin{aligned}\mathcal{S}_{\hat{d}}\big(f(k)\big) \to \big\{&\mathcal{S}_{\hat{d}l}\big(f(k-jA+z)\big),\\ &\mathcal{S}_{\hat{d}r}\big(f(k+jA-z)\big),\mathcal{S}_{\hat{d}m}\big(f(k)\big)\big\}.\end{aligned} \tag{27}$$

This leaves us with the Fourier and inverse Fourier transformations. The forward transformation is implemented by the following steps.

1. The spatial data is transformed with the transformation implemented for the Hermite discretization. The result is stored in the main data object.
2. The main data object is re-sampled on the left and right discretization with the real shift $\pm z$ applied.
3. The side data objects are transformed back to the spatial domain.
4. The side data functions are multiplied by exponential functions to apply the (spectral) imaginary shift $A$.
5. The side data functions are transformed to the spectral domain for a final time.

In formulas, this algorithm is given by:

$$\begin{aligned}\hat{\mathbb{f}}_{\hat{d}m} &= \mathcal{F}_{dm}\Big\{\mathbb{f}_{dm}\Big\}\\ \hat{\mathbb{f}}_{\hat{d}l} &= \mathcal{F}_{dl}\Big\{\mathcal{F}^{-1}_{\hat{d}l}\Big\{\mathcal{R}_{dl}(\hat{\mathbb{f}}_{\hat{d}m},-z)\Big\}\cdot\mathbb{e}^{(1)}_{dl}\Big\}\\ \hat{\mathbb{f}}_{\hat{d}r} &= \mathcal{F}_{dr}\Big\{\mathcal{F}^{-1}_{\hat{d}r}\Big\{\mathcal{R}_{dr}(\hat{\mathbb{f}}_{\hat{d}m},z)\Big\}\cdot\mathbb{e}^{(2)}_{dr}\Big\}.\end{aligned} \tag{28}$$

The inverse Fourier transformation recombines these three spectral data objects into a single spatial data object. This procedure is described by the following steps.

1. The data objects are multiplied by their corresponding selection functions.
2. The inverse Fourier transformation is performed on the individual data objects after multiplication. This results in three spatial data objects.
3. The side data objects are re-sampled on the main discretization object, so they can be combined.
4. The complex spectral shifts are reversed by multiplying by their complementary exponential functions (Eq. (30)).
5. The resulting data objects are added.

This algorithm implements Eq. (13) for the CDO. In formula form it is described by

$$\begin{aligned}\mathbb{f}_{dm} \;=\; &\mathcal{F}^{-1}_{\hat{d}m}\Big\{\hat{\mathbb{s}}_{\hat{m}}\cdot\hat{\mathbb{f}}_{\hat{m}}\Big\} + \mathbb{e}^{(3)}_{dm}\cdot\mathcal{R}_{dm}\left(\mathcal{F}^{-1}_{\hat{d}l}\Big\{\hat{\mathbb{s}}_{\hat{d}l}\cdot\hat{\mathbb{f}}_{\hat{d}l}\Big\}\right)\\ &+\mathbb{e}^{(4)}_{dm}\cdot\mathcal{R}_{dm}\left(\mathcal{F}^{-1}_{\hat{d}r}\Big\{\hat{\mathbb{s}}_{\hat{d}r}\cdot\hat{\mathbb{f}}_{\hat{d}r}\Big\}\right),\end{aligned} \tag{29}$$

with

$$\begin{aligned} \mathfrak{e}_{dm}^{(3)} &= \mathcal{S}_{dm}\big(\exp((A+jz)x)\big), \\ \mathfrak{e}_{dm}^{(4)} &= \mathcal{S}_{dm}\big(\exp(-(A+jz)x)\big). \end{aligned} \tag{30}$$

## 4. CHOICE OF PARAMETERS

### 4.1. Implementation

The discretization method discussed in the previous section was implemented in C++. It was compiled with gcc as a module to be used by a Python (version 3.7) frontend. All results in this work were obtained on a computational server containing an AMD EPYC 7573X as its processor. All the calculations were done on a single thread without any parallelization. The operating system is Ubuntu 22. Finally, the plots made for this work have been generated using the Matplotlib library [18].

### 4.2. The Spatial Spectral Solver Parameters

The solver requires a set of discretization parameters, see Table 3, to be specified. The aim in choosing these parameters is to achieve an acceptable compromise between computational efficiency and accuracy. In analysing the considerations to be made for these choices, we will assume the same parameter values for both discretization dimensions. We will also use the same parameters for both left and right discretization objects and will refer to them collectively as the "side" discretization objects.

**TABLE 3**. Parameters for the CDO.

| Hermite-based composite discretization | Spatial | Spectral |
|---|---|---|
| Sample distance main | $\Delta_x^m$ | $\Delta_k^m$ |
| Sampling range main | $r_x^m$ | $r_k^m$ |
| Sample distance side | $\Delta_x^s$ | $\Delta_k^s$ |
| Sampling range side | $r_x^s$ | $r_k^s$ |
| Interpolation order | d | d |
| Imaginary shift | - | A |
| Selection function start | - | $S_0$ |
| Selection function width | - | $S_w$ |
| Selection function transition width | - | $S_t$ |
| Selection function transition steepness | - | $\alpha$ |

### 4.3. Domain Sizes

When using the solver we specify the spatial parameters and let the dual spectral discretization objects be automatically derived from them. However for the purposes of analysis, it is generally more insightful to consider both spatial and spectral domain sizes, instead of spatial domain sizes and sampling distances. We will therefore primarily use this framing and use Eq. (14) when conversion is necessary.

The core of the solver is built around the use of convolution with a Green function to determine the scattered field. Although this convolution is performed, in practice, as a multiplication in the spectral domain, the information content still has to be identical to that of the spatial domain. In other words, we cannot have a spectral representation that contains less information than its spatial counterpart and still expect accurate results.

The 2D TE Green function, given by (5), has an infinite support, meaning that the convolution integral also has an infinite support. However, in practice we only require the contrast current on the (compactly supported) dielectric scatterer. For a scatterer supported on $x = -D$ to $x = D$, it is readily verified that the resulting field on the scatterer only requires the Green function values from $-2D$ to $2D$.

### 4.4. Selection functions

The selection functions are what enables the combinations of the different paths and should therefore be considered in more detail. The functions $\hat{s}_l$, $\hat{s}_r$, and $\hat{s}_m$ can be expressed in terms of each other, so for this section we will only consider $\hat{s}_r$. This function takes on a value of $\sim 1$ around the singularity at $k_0$, while it vanishes outside this region with a smooth transition between these extremes. We use a symmetric function that is fully determined by four parameters:

1. $S_0$, the start of the transition from 0 to 1.
2. $S_w$, the total width of the selection function.
3. $S_t$, the width of the transition region.
4. $\alpha$, a factor determining the steepness of the transition.

The selection function we use can be described by

$$s_r = f_s(k, S_0, S_0 + S_t, \alpha) f_s(k, S_0 + S_t, S_0 + S_w - S_t, \alpha), \tag{31}$$

where

$$f_s(k, a, b, \alpha) = \begin{cases} 0 & \text{if } k \le a, \\ 1 & \text{if } k \ge b, \\ \frac{1}{2}\left(1 - \frac{\operatorname{erf}\left(\alpha\left(\frac{k-b}{a-b} - \frac{1}{2}\right)\right)}{\operatorname{erf}\left(\frac{1}{2}\alpha\right)}\right), & \text{else.} \end{cases} \tag{32}$$

For the analysis, we assumed that the selection functions are analytic. However, there are no (non-constant) analytic functions that are strictly 0 on an open interval. Instead, this function is a good approximation for the product of two error functions, which is analytic. We employ this function under the assumption that it is numerically close enough to the analytic function, such that the approximations involved in the integration paths of the Fourier transform are controllably small. This assumption is shown to hold in Section 5.

### 4.5. Shifting the Side Discretization Objects

The selection functions allow us to only consider a small part of the spectral domain for the side discretization objects. However, in our implementation a function is sampled symmetrically around the origin. This is done so all the data objects share the same underlying grid. Since the side discretization objects are only non-zero around $\pm k_0$, this is wasteful because functions would need to be sampled for at least $k \in [-k_0 - S_t, k_0 + S_t]$, see Fig. 5.

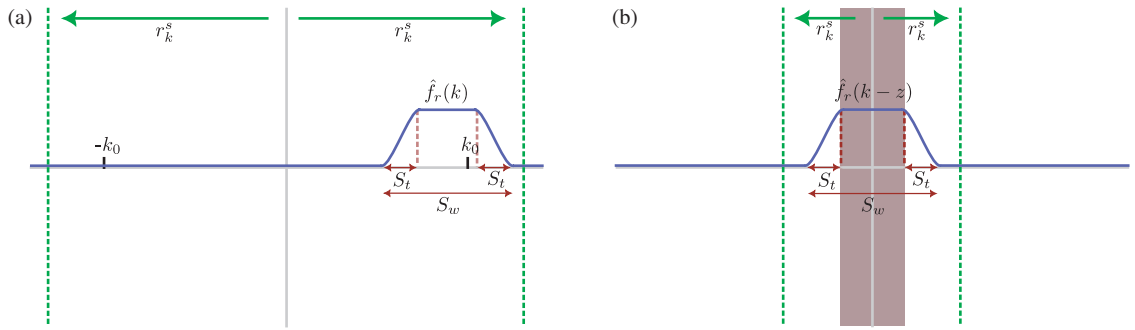


**FIGURE 5**. (a) Most of the side discretization objects' space is wasted since any data is suppressed by the selection function outside a small bounded region. (b) By adding the real shift $z$, we only require a fraction of the original discretization range. For a proper discretization we should have $k_0 - z$ inside $[-r_k^s, r_k^s]$.

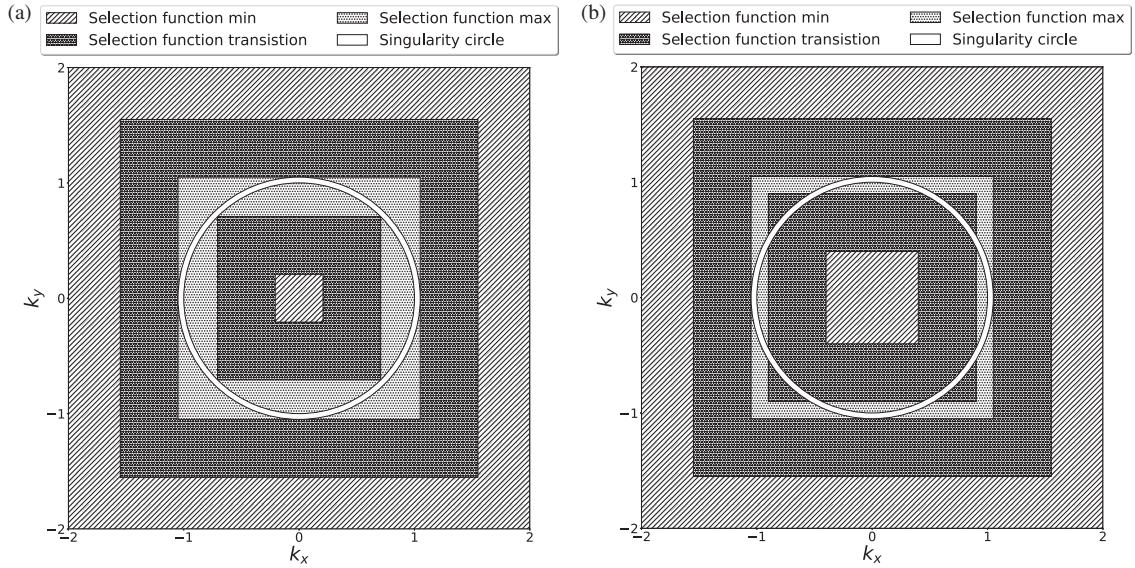


**FIGURE 6**. (a) When the selection functions are not broad enough, they may not be able to contain the entire circle of the singular behavior in the 2D Green function. (b) The Green function in two dimensions has its singularity on a circle in the complex plane. For the selection functions to contain all these locations puts a restriction on the effective width of the selection functions.

To reduce the amount of redundant sample points, we add a real shift $z = -S_0 + \frac{1}{2}S_w$ to the functions on the side representations, such that they become centered around the origin. This leads to a reduction in the minimum spectral discretization range from $r_k^s \geq k_0 + S_t$ to $r_k^s \geq \frac{1}{2}S_w$.

### 4.6. The Width of the Selection Functions in the 2D Problem

The selection functions restrict the spectral discretization range $r_k^s$ of the side objects. A narrow selection function results in a small value for $r_k^s$. However, the functions still need to be wide enough to always contain the singularities at $k = \pm k_0$. Since the scattering problem is two-dimensional, the singularities in the spectral domain do not just lie on discrete points, but instead lie on a circle with radius $k_0$, as indicated in Fig. 6. This leads to a minimum width of the selection functions:

$$S_w \geq \frac{\sqrt{2}-1}{\sqrt{2}} k_0 + 2S_t, \tag{33}$$

which only leaves us with a choice for the transition region width $S_t$ and transition steepness parameter $\alpha$.

### 4.7. Main Discretization Spatial Range

The composite path representation of the Green function confines the contributions of the spectral singularities to the side discretization objects. This means that we can expect the long-range behavior of the Green function to be relegated to the side discretizations as well. This, in turn, implies the spatial content of the Green function represented on the main discretization object has a limited effective support.

In Fig. 7, we see the spectral Green function in the same plot as the same function suppressed by the selection function $\hat{s}_m$. We see that the multiplication removes the steep sections around the singularities. The transition regions of $\hat{s}_m$ now have the sharpest behavior of the function and therefore dictate the decay of the function in the spatial domain. We see this in effect in Fig. 8 for an example set of discretization parameters.

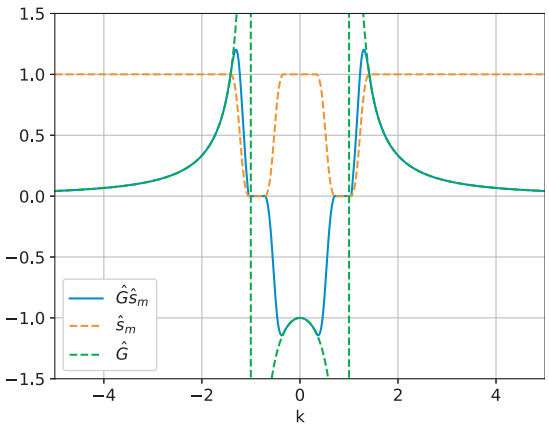


**FIGURE 7**. An example of the effect of applying the main selection function to the spectral Green function. The steepest part that are present in the remaining function are in the transition regions. Used parameter values: $S_0 = 0.35$, $S_t = 0.35$, $S_w = 1.055$ and $\alpha = 3.5$.

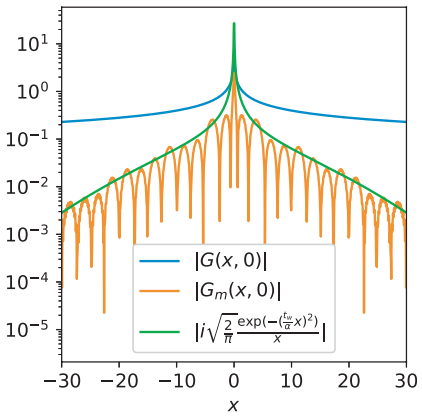


**FIGURE 8**. The absolute value of $G([x,0]^T)$ and $\mathcal{F}^{-1}\left\{\hat{s}_m\hat{G}\right\}([x,0]^T)$, for the same discretization parameters used for Fig. 7. We see the latter decay significantly faster, which allows for truncation of the discretization domain. We also see that the Green function decay follows the predicted behavior.

The transition regions of the selection functions are described by scaled error functions with analytic inverse Fourier transformation [19, Eq. 29.3.113]:

$$\mathcal{F}^{-1}\left\{\frac{\operatorname{erf}(\frac{\alpha}{S_t}k)}{\operatorname{erf}(\frac{1}{2}\alpha)}\right\} = -j\sqrt{\frac{2}{\pi}}\frac{\exp(-(\frac{S_t}{2\alpha}x)^2)}{x\operatorname{erf}(\frac{1}{2}\alpha)}. \quad (34)$$

So the Green function on the main discretization object decays super-exponentially, meaning that we can truncate it to some effective width $R_G$. This leaves the required spatial range to be $r_x^m = R_G + D$ which for large scatterers ($D > R_G$) improves the $r_x^m = 2D$ bound established for a general convolution.

### 4.8. Main Discretization Spectral Range

The only hard requirement for the spectral range of the main discretization, and therefore indirectly the spatial sampling distance, is that the selection function $\hat{s}_m$ is contained within its support. This imposes the bound that $r_k^m > S_0 + S_w$. This bound requires sampling just slightly finer than the Nyquist limit, which is already a requirement for simulations of this nature. Within this bound $\Delta_x^m$ can be treated as a free variable.

### 4.9. Side Discretization Spatial Range

We want to solve Eq. (8) using the composite path representation. This means that on the side discretization the Green function is multiplied with the contrast current and the relevant selection function in the spectral domain Eq. (11). This corresponds to a double convolution in the spatial domain:

$$\mathcal{F}^{-1}\left\{\hat{G}(k-jA)\hat{s}_l(k-jA)\hat{J}(k-jA)\right\}$$
$$= 2\pi k_0^2 e^{-Ax}G(x) * (s_l(x) * J(x))). \quad (35)$$

The support of the inner convolution is equal to the sum of the support of its components $R_G + D$. Since we only need the resulting fields on the scatterer, the second convolution implies that we need $r_x^s = R_G + 2D$.

### 4.10. Complex Shift

The imaginary shift $A$ is relevant both for data on the side discretization objects and for the selection functions. As shown in Fig. 9, increasing $A$ causes the selection functions to increase rapidly, which makes them harder to represent by means of the Hermite interpolation and can therefore lead to numerical errors. In contrast, the Green function is actually better behaved for large values of $A$, see Fig. 10. Since the product of both functions is needed, a trade-off for $A$ is required.

The accuracy of the representation for the Green function and the selection functions is limited by how fine we sample in the spectral domain, since steeper functions require either a denser sampling rate or a higher polynomial degree for the interpolation. From these considerations, we make the practical choice $A = \Delta_k^s$, which seems to perform well over a wide range of simulations and agrees with the work reported in [9].

## 5. RESULTS FOR A 2D SCATTERER

The units in the simulations are based on a normalized wavenumber of $k_0 = 1$.

To test the composite discretization objects (CDOs), we use them to solve 3 types of problems:

1. A plane wave incident on a small dielectric cylinder.
2. A plane wave incident on a large dielectric cylinder.
3. A plane wave incident on a lens with a high dielectric contrast.

The first two cases have an analytical reference which is used to quantify the errors. For all three cases, we use a spectral-deformation-based discretization to compare speed and accuracy. These scatterers are used both because of the available analytical reference and because they have simple spectral descriptions. In principle, any dielectric scatterer, including non-homogeneous ones, could be used in exactly the same manner assuming that a spectral representation can be constructed [20].

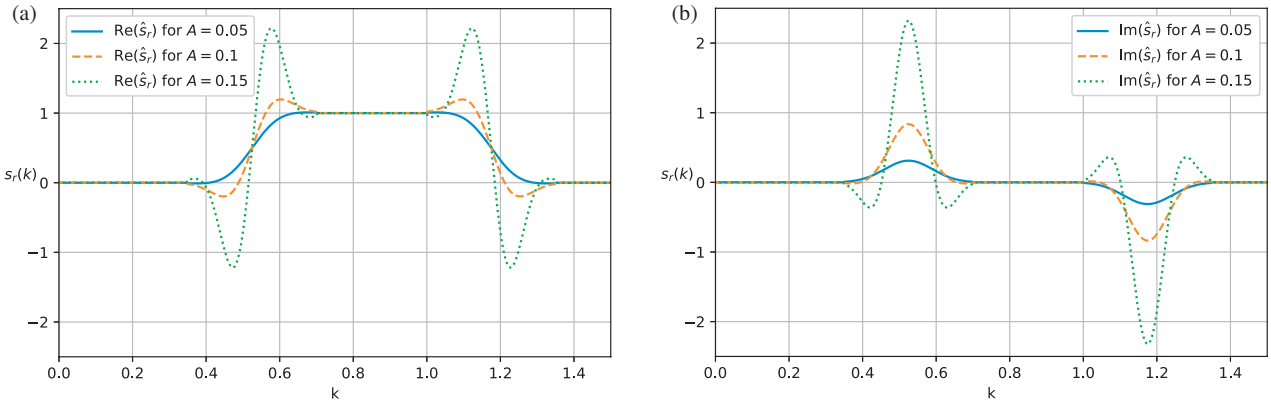


**FIGURE 9**. An example of a selection function with a complex shift evaluated over the real $k$ axis. We plot the (a) real and (b) imaginary parts of the functions for 3 for different values of $A$. The selection functions start showing oscillatory behavior at the edges as $A$ increases, which makes the representation by the polynomial Hermite interpolation more challenging and leads to an increase in numerical errors.

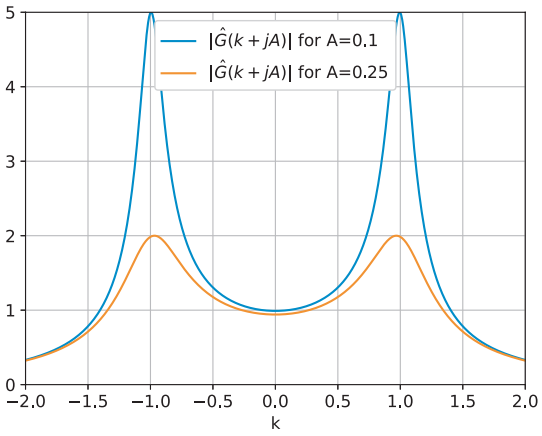


**FIGURE 10**. Unlike the selection functions, the Green reduces in steepness for larger $A$.

### 5.1. Comparison with Spectral Deformation Discretization

We implemented the deformed spectral path method from [9] as a discretization object, with Hermite discretization as the underlying method. We use results obtained from this method as a comparison for the CDO based approach. This provides a good benchmark for the error and performance since it uses the same underlying Hermite discretization and offers the same flexibility in discretization since both methods avoid direct discretization of the spectral Green function singularities. The spectral deformation discretization does this using a Taylor expansion, in this case of order 8. This means that 8 Fourier transformations are required in the underlying discretization for a single path-deformed Fourier discretization, which is computationally heavy. Additionally, the CDO method requires a smaller spatial discretization domain since it only needs to contain the scatterer plus some constant offset for the Green function, instead of twice the scatterer size.

The Hermite parameters we use for the reference discretization will be identical to those of the main discretization object of the CDO. The imaginary shift $A$ will also be the same for both discretizations.

### 5.2. Setting up the Solver

To obtain the solutions to Eq. (8) we employ an iterative solver, specifically GMRES [21]. The discretized representation of the problem is given by

$$B\mathbb{x}_d = \mathbb{x}_d - 2\pi\mathcal{F}_{\hat{d}}^{-1}\left\{\hat{\mathbb{G}}_{\hat{d}}\mathcal{F}_d\left\{\mathbb{\Pi}_d\mathbb{x}_d\right\}\right\} = \mathbb{E}_d^i. \tag{36}$$

To implement the matrix-vector product regarding the matrix $B$, we require the representations of the spectral Green function $\hat{\mathbb{G}}_{\hat{d}}$ and the spatial representation of the scatterer $\mathbb{\Pi}_d$. Furthermore, we need a representation of the incident wave for which we use an incident plane wave of the form

$$\mathbb{E}_d^i = \mathcal{S}_d\{\exp(j(\cos(\theta^i)x + \sin(\theta^i)y))\}, \tag{37}$$

with the angle of incidence $\theta^i$.

The scatterer has a compact support. If this scatterer were to be sampled spatially, the boundaries of the resulting object would be very sensitive to the simulation parameters due to the sharp nature of the edges. Instead, to ensure a more consistent result, we sample a spectral version and transform it to the spatial domain. This does add some error due to the Gibbs phenomenon, but it leads to a consistent representation that is less sensitive to specific discretization parameters [20]. The simulations are performed following these steps:

1. Initialize the CDO.
2. Sample the Green function in the spectral domain.
3. Sample the dielectric scatterer in the spectral domain and transform it to the spatial domain.
4. Sample the incident plane wave in the spatial domain.
5. Use GMRES to find the solution with a residual error smaller than $1 \times 10^{-5}$ and use the incident field as the starting vector.

### 5.3. Homogeneous Dielectric Circular Cylinder

To test the CDO based method, we start with a simple case: a homogeneous dielectric cylinder (Case 1), illuminated by an

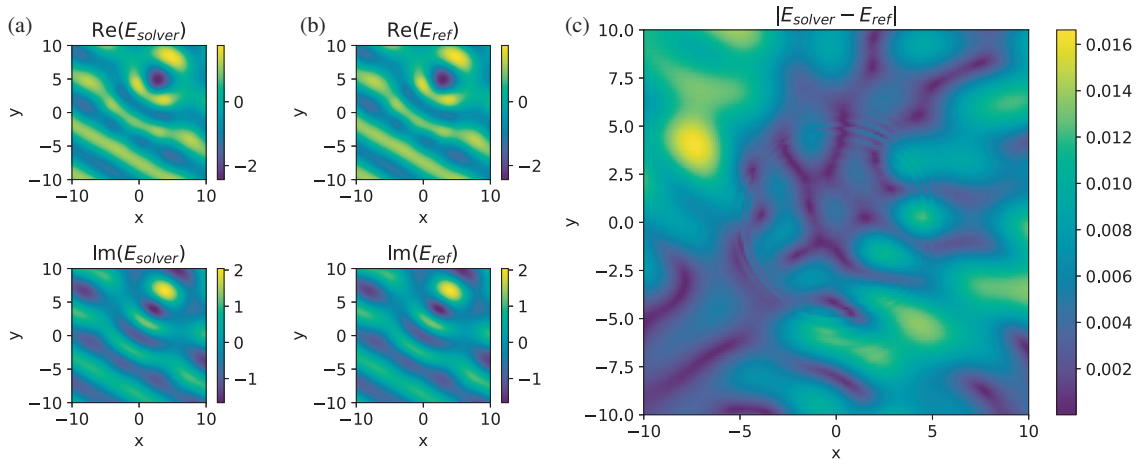


**FIGURE 11**. The resulting field for (a) the CDO based method, (b) the analytical reference and (c) the absolute difference between these two computed fields.

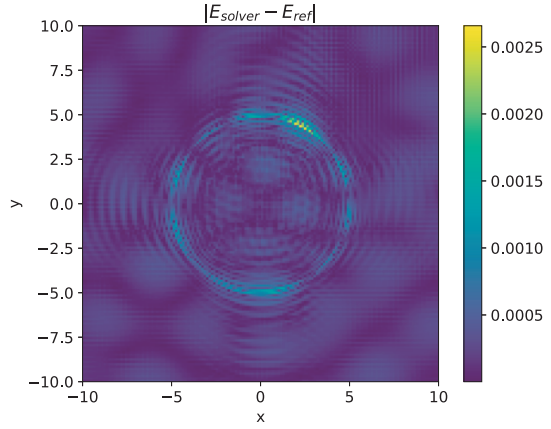


**FIGURE 12**. By increasing $r_x^m$, $r_x^s$ and by decreasing $\Delta_x^s$ we obtain smaller errors at the cost of more computational resources as compared to Fig. 11.

$E$-polarized plane wave, for which an analytical reference [22] is available to quantify the accuracy.

The characteristic function of a circle in the spatial domain, with radius $\rho$ and center position $\vec{x_c}$, has the following spectral-domain counterpart:

$$\hat{\xi}_{\rho}^{(\vec{x_c})}(\vec{k}) = \begin{cases} \frac{\rho^2}{2} \text{ if } k_r = 0, \\ \frac{\rho}{k_r} \exp[j(x_c k_x + y_c k_y)] J_1(k_r \rho) \text{ else,} \end{cases} \tag{38}$$

where $k_r = \left(k_x^2 + k_y^2\right)^{0.5}$ and $J_1$ is the Bessel function of the first kind of order one. For the cylinder test cases we choose $\vec{x_c} = \vec{0}$. The parameters for the simulation can be found in the third column in Table 4.

The resulting total fields are shown in Fig. 11 (using a value of $r_x^m = 15$). We see that the calculated fields match the analytical reference with a relative $L^2$ norm of $7.2 \times 10^{-3}$ and a maximum deviation smaller than $2 \times 10^{-2}$.

In Fig. 13, we show the relative error with respect to the reference for increasing discretization range, $r_x^m$ and $r_x$, for the CDO based method and spectral deformation method, respectively. We see similar results in both accuracy and time taken due to the small size of the scatterer. This is because for the CDO based method we require $r_x^m \geq \rho + R_G$ and $r_x^s \geq 2\rho + R_G$ whereas the deformed path method needs $r_x \geq 2\rho$. However, for larger simulation domains the CDO based method performs better, since $R_G < \rho$, which yields a smaller main discretization. The computational effort on the side-discretizations is much smaller owing to the coarser discretization. We note here that these errors are not the best the method can do. In Fig. 12, we show the resulting absolute error for the same scatterer and incident field, where we have instead chosen $\Delta_x^s = 1$, $r_x^m = 100$, and $r_x^s = 110$. With these parameters we bring down the relative $L^2$ norm to $2.5 \times 10^{-4}$, and the largest re-

**TABLE 4**. Simulation parameters for the different setups. For case 1 and 2 the value varies.

| Simulation parameters | | Case 1 | Case 2 | Case 3 |
|---|---|---|---|---|
| Angle of incidence | $\theta^i$ | $\frac{\pi}{3}$ | $\frac{\pi}{3}$ | $\frac{\pi}{2}$ |
| Radius | $\rho$ | 5 | 50 | 201 |
| Relative permittivity | $\epsilon_r$ | 2 | 1.1 | 10 |
| Wavenumber | $k_0$ | 1 | 1 | 1 |
| Hermite parameters | | | | |
| Main discretization range | $r_x^m$ | - | - | 20 |
| Side discretization range | $r_x^s$ | 40 | 130 | 40 |
| Main discretization step | $\Delta_x^m$ | 0.3 | 0.3 | 0.5 |
| Side discretization step | $\Delta_x^s$ | 3.5 | 3 | 3 |
| Interpolation degree | $d$ | 3 | 3 | 3 |
| Selection function parameters | | | | |
| Steepness | $\alpha$ | 3.5 | 3.5 | 3.5 |
| Start | $S_0$ | 0.1 | 0.1 | 0.35 |
| Width | $S_w$ | 1.5 | 1.5 | 1.35 |
| Transition width | $S_t$ | 0.5 | 0.5 | 0.35 |
| Imaginary shift | $A$ | 0.079 | 0.024 | 0.079 |

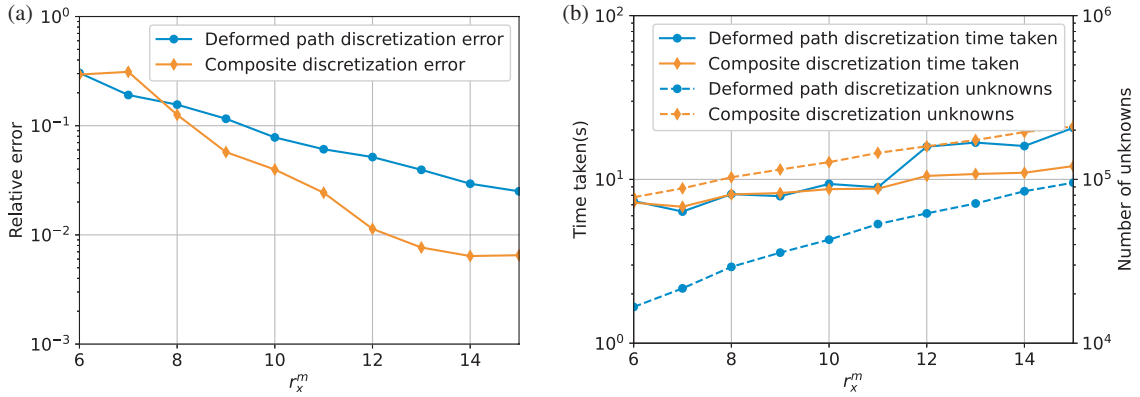


**FIGURE 13**. Error, timing, and number of unknowns comparison for a homogeneous dielectric circular-cylindrical scatterer with radius $\rho = 5$ and $\epsilon_r = 2$. (a) The relative errors with respect to the analytical reference. (b) The computation time and the number of unknowns. Both figures involve the CDO and the spectral path deformation discretization objects.

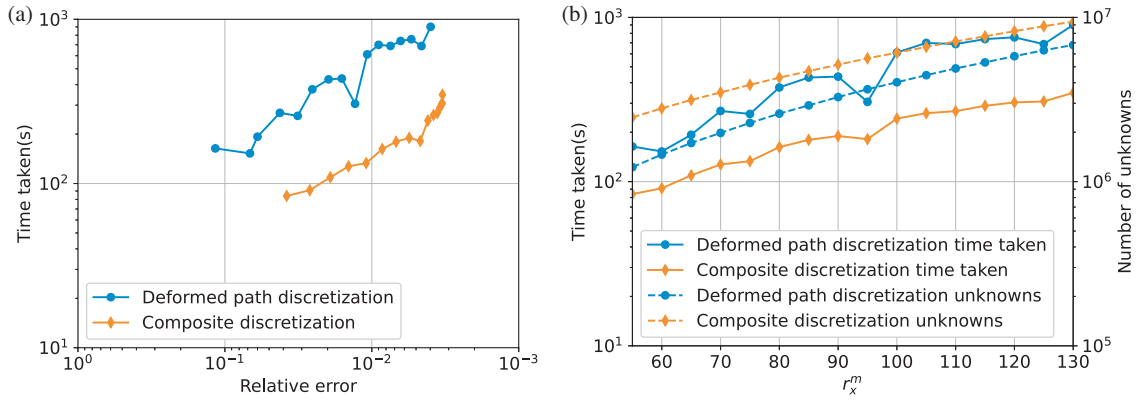


**FIGURE 14**. Comparison of achieved relative error against the time taken to run the solver for a for a homogeneous dielectric circular-cylindrical scatterer with radius $\rho = 50$ and $\epsilon_r = 1.1$ (a) for both the CDO and the spectral path deformation discretization objects. The computation time and the number of unknowns (b) for both methods.

maining deviations are now smaller than $2.5 \times 10^{-3}$ and are concentrated around the edge of the scatterer. It is clear that the remaining errors are of a different nature than that of Fig. 11 and are dominated by other parameters. Solving this system now takes 744 s, roughly a 50 times increase in computation time compared to the most time-consuming simulation data point in Fig. 13. Since our primary interest lies in obtaining a balance among computational efficiency, accuracy, and flexibility, we will keep using the faster, but less accurate, simulation settings from here on.

When we consider a larger cylinder (Case 2), we observe the expected gain in computational efficiency. In Fig. 14, we show the achieved relative error vs computation time for a homogeneous dielectric circular cylinder with radius $\rho = 50$ and $\epsilon_r = 1.1$. From this graph it is clear that the CDO based method is the more efficient choice for a setup of this size. It is important to note that the CDO based method does have a larger number of unknowns for a given $r_x$, but this is nullified by the gain in accuracy. In the bottom graph, it can be seen that for a given accuracy the CDO based method requires less computation time. This improvement in efficiency indicates the successful separation of long-distance behavior of the Green function in the side-discretizations and the short-distance behavior of the Green function in the main discretization for the CDO. Therefore, the main discretization, which carries the main workload of the method, now has $r_x^m$ smaller than twice the radius of the scatter. The full set of simulation parameters is listed in the fourth column of Table 4.

### 5.4. Results for a Dielectric Lens

As a final demonstration, we consider a plane wave incident on a dielectric lens (Case 3). We take an $E$-polarized plane wave incident on a homogeneous dielectric lens that focuses the field into a beam. Again, we compare the results for both methods. For the lens geometry we use the (spatial) intersection of the interior of two circles with the same radius. As discussed above, we perform the sampling of the scatterer in the spectral domain. By multiplying the characteristic functions of two circles with different center positions, we obtain the characteristic function of a lens in the spatial domain. This allows us to create an object that represents the characteristic function of a lens with permittivity $\epsilon_r$ on a discretization object $d$ as:

$$\mathbb{\Pi}_d(\vec{x}) = (\epsilon_r - 1)\mathcal{F}_{\hat{d}}^{-1}\left\{\mathcal{S}_c\left(\hat{\xi}_{\rho_1}^{\vec{x}_1}\right)\right\}\mathcal{F}_{\hat{d}}^{-1}\left\{\mathcal{S}_c\left(\hat{\xi}_{\rho_2}^{(\vec{x}_2)}\right)\right\}. \quad (39)$$

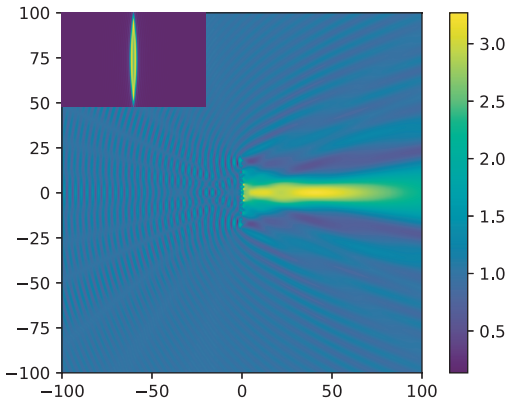


**FIGURE 15**. A dielectric lens (with $\epsilon_r = 10$ focuses the incident field, arriving from the left-hand side, into a beam. The figure depicts the total electric field. The inset at the top-left depicts the lens without any fields.

The information pertaining to the long-range spatial interactions is contained in the side discretization objects. This means that the main discretization object only needs to be large enough to contain the lens and a distance $R_G$ around it. Once the simulation is run, we can demonstrate the lens focusing the resulting field by re-sampling the calculated (compact) contrast current density on a discretization object with a larger extent and by applying the forward scattering operation. The parameters for this simulation are found in the fifth column of Table 4. In Fig. 15, the resulting total field from this setup for the CDO is shown.

In Table 5, we show the relative difference, with respect to the spectral path deformation method and the corresponding computation times for a set of lenses, each with a different permittivity and for various levels of coarseness on the side discretizations. The full simulation was performed for each setting, even though the deformation method does not depend on $\Delta_x^s$. The simulations were performed five times, and of these results the shortest achieved computation time is displayed. The relative difference between the results of the two methods is smaller than $5 \times 10^{-2}$. From these results the improvement in computation speed of the CDO method is demonstrated. The two methods arrive at similar resulting fields, but the CDO is between 2 and 3 times faster than the path deformation method for all the tested cases.

## 6. CONCLUSION

We introduced a method to represent the frequency-domain 2D spectral Green function for a homogeneous medium of infinite extent on three separate complex paths by employing appropriate selection functions. Using this formulation, we developed a software framework to solve 2D $E$-polarized dielectric scattering problems.

The resulting framework with a CDO was used to solve scattering problems for two types of dielectric scatterers, i.e., a homogeneous dielectric circular cylinder and a homogeneous dielectric lens. The CDO based method keeps the discretization of the Green function simple, since we never sample close to the Green-function singularities. This gives it the same flexibility in discretization as a previously used method that utilizes a single complex-deformed path in the spectral domain.

**TABLE 5**. Comparison between the CDO based method and the spectral deformation method for a dielectric lens with several values for $\epsilon_r$ and for several sample distances $\Delta_x^s$.

| | Time (CDO) | Time (Deformation) | Relative error (Deformation ) as reference |
|---|---|---|---|
| $\epsilon_r = 2,\ \Delta_x^s = 2$ | 7.4 s | 15.7 s | $3.36 \times 10^{-2}$ |
| $\epsilon_r = 2,\ \Delta_x^s = 3$ | 6.77 s | 15.6 s | $3.35 \times 10^{-2}$ |
| $\epsilon_r = 2,\ \Delta_x^s = 4$ | 5.38 s | 15.5 s | $3.45 \times 10^{-2}$ |
| $\epsilon_r = 2,\ \Delta_x^s = 5$ | 5.30 s | 15.6 s | $3.34 \times 10^{-2}$ |
| $\epsilon_r = 5,\ \Delta_x^s = 2$ | 23.1 s | 48.2 s | $4.46 \times 10^{-2}$ |
| $\epsilon_r = 5,\ \Delta_x^s = 3$ | 24.0 s | 48.7 s | $4.44 \times 10^{-2}$ |
| $\epsilon_r = 5,\ \Delta_x^s = 4$ | 17.8 s | 47.3 s | $4.35 \times 10^{-2}$ |
| $\epsilon_r = 5,\ \Delta_x^s = 5$ | 16.9 | 46.0 s | $4.40 \times 10^{-2}$ |
| $\epsilon_r = 10,\ \Delta_x^s = 2$ | 50.4 s | 102 s | $2.21 \times 10^{-2}$ |
| $\epsilon_r = 10,\ \Delta_x^s = 3$ | 45.7 s | 103 s | $2.10 \times 10^{-2}$ |
| $\epsilon_r = 10,\ \Delta_x^s = 4$ | 38.6 s | 104 s | $2.07 \times 10^{-2}$ |
| $\epsilon_r = 10,\ \Delta_x^s = 5$ | 36.6 s | 103 s | $2.08 \times 10^{-2}$ |

By using these separate paths, the part of the Green function that corresponds to long-range interactions is treated separately from the parts with short-range interactions. We showed that the split in representation allows for a reduction in the spatial discretization range for the largest part of the spectral domain on which only the short-range interaction works. On the other hand, the side-discretizations that contain the spectral-domain singularities require a larger spatial-domain path, since they represent the long-range interaction. Since the side discretizations only require a very coarse spatial sampling, these side-discretizations are still rather efficient. Together, this leads to an overall reduction in the number of unknowns and in computation time as compared to previous work.

## REFERENCES

[1] Inan, U. S. and R. A. Marshall, *Numerical Electromagnetics: The FDTD Method*, Cambridge University Press, 2011.

[2] Sankaran, K., "Are you using the right tools in computational electromagnetics?" *Engineering Reports*, Vol. 1, No. 3, e12041, 2019.

[3] Jin, J.-M., *The Finite Element Method in Electromagnetics*, John Wiley & Sons, 2015.

[4] Zwamborn, P. and P. M. van den Berg, "The three dimensional weak form of the conjugate gradient FFT method for solving scattering problems," *IEEE Transactions on Microwave Theory and Techniques*, Vol. 40, No. 9, 1757–1766, 1992.

[5] Bojarski, N. N., "The k-space formulation of the scattering problem in the time domain," *The Journal of the Acoustical Society of America*, Vol. 72, No. 2, 570–584, 1982.

[6] Van Beurden, M. C., "Fast convergence with spectral volume integral equation for crossed block-shaped gratings with improved material interface conditions," *Journal of the Optical Society of America A*, Vol. 28, No. 11, 2269–2278, 2011.

[7] Dilz, R. J. and M. C. van Beurden, "An efficient spatial spectral integral-equation method for EM scattering from finite objects in layered media," in *2016 International Conference on Electromagnetics in Advanced Applications (ICEAA)*, 509–511, Cairns, QLD, Australia, Sep. 2016.

[8] Dilz, R. J. and M. C. van Beurden, "An efficient complex spectral path formulation for simulating the 2D TE scattering problem in a layered medium using Gabor frames," *Journal of Computational Physics*, Vol. 345, 528–542, 2017.

[9] Dilz, R. J. and M. C. van Beurden, "A Hermite-interpolation discretization and a uniform path deformation for the spatial spectral domain integral equation method in multilayered media for TE polarization," *Progress In Electromagnetics Research B*, Vol. 80, 37–57, 2018.

[10] Michalski, K. A. and J. R. Mosig, "Efficient computation of Sommerfeld integral tails — Methods and algorithms," *Journal of Electromagnetic Waves and Applications*, Vol. 30, No. 3, 281–317, 2016.

[11] Sommerfeld, A., "Über die ausbreitung der wellen inder drahtlosen telegraphie," *Annalen Der Physik*, Vol. 333, 665–736, 1909.

[12] Michalski, K. A. and J. R. Mosig, "The Sommerfeld half-space problem revisited: From radio frequencies and Zenneck waves to visible light and Fano modes," *Journal of Electromagnetic Waves and Applications*, Vol. 30, No. 1, 1–42, 2016.

[13] Ewald, P. P., "Die berechnung optischer und elektrostatischer gitterpotentiale," *Annalen Der Physik*, Vol. 369, No. 3, 253–287, 1921.

[14] Jordan, K. E., G. R. Richter, and P. Sheng, "An efficient numerical evaluation of the Green's function for the Helmholtz operator on periodic structures," *Journal of Computational Physics*, Vol. 63, No. 1, 222–235, 1986.

[15] Dilz, R. J., M. G. M. M. van Kraaij, and M. C. van Beurden, "A 3D spatial spectral integral equation method for electromagnetic scattering from finite objects in a layered medium," *Optical and Quantum Electronics*, Vol. 50, No. 5, 206, 2018.

[16] Waterman, P. C., "The T-matrix revisited," *Journal of the Optical Society of America A*, Vol. 24, No. 8, 2257–2267, Aug. 2007.

[17] Richmond, J., "Scattering by a dielectric cylinder of arbitrary cross section shape," *IEEE Transactions on Antennas and Propagation*, Vol. 13, No. 3, 334–341, 1965.

[18] Hunter, J. D., "Matplotlib: A 2D graphics environment," *Computing in Science & Engineering*, Vol. 9, No. 3, 90–95, 2007.

[19] Abramowitz, M. and I. A. Stegun, *Handbook of Mathematical Functions with Formulas, Graphs, and Mathematical Tables*, US Government Printing Office, 1968.

[20] Eijsvogel, S., L. Sun, F. Sepehripour, R. J. Dilz, and M. C. van Beurden, "Describing discontinuous finite 3D scattering objects in Gabor coefficients: Fast and accurate methods," *Journal of the Optical Society of America A*, Vol. 39, No. 1, 86–97, 2022.

[21] Saad, Y. and M. H. Schultz, "GMRES: A generalized minimal residual algorithm for solving nonsymmetric linear systems," *SIAM Journal on Scientific and Statistical Computing*, Vol. 7, No. 3, 856–869, 1986.

[22] Van de Water, A. M., "LEGO: Linear embedding via Green's operators," Ph.D. dissertation, PhD Thesis 1 (Research TU/e/Graduation TU/e), Electrical Engineering, Eindhoven University of Technology, Eindhoven, The Netherlands, 2007.